PHYSICAL REVIEW FLUIDS **9**, 054603 (2024)

Low-frequency unsteadiness in hypersonic swept shock wave-boundary layer interactions

Alessandro Ceci,[1,*] Andrea Palumbo,[1] Johan Larsson,[2] and Sergio Pirozzoli[1]
[1]*Dipartimento di Ingegneria Meccanica e Aerospaziale, Sapienza Università di Roma, Via Eudossiana 18, 00184 Rome, Italy*
[2]*Department of Mechanical Engineering, University of Maryland, College Park, Maryland 20742, USA*

(Received 14 November 2023; accepted 5 April 2024; published 7 May 2024)

We carry out a numerical study of swept shock wave/turbulent boundary layer interaction in the hypersonic regime. Starting from a numerical/experimental benchmark case of a nearly adiabatic two-dimensional hypersonic interaction, a crossflow velocity component is added to the incoming flow to mimic three-dimensional interactions with cylindrical symmetry. We observe, for a fixed streamwise Mach number, monotonic increase of the extent of the interaction region for the swept cases. An attempt at extending the free-interaction theory to hypersonic swept interactions is made, which is found to apply only to the initial part of the interaction region. The spatiotemporal dynamics of wall pressure on mean separation line features large-scale pressure corrugations, which are advected at a phase speed which is a fraction of the mean crossflow velocity, if present. The characteristic wavelength of the corrugation is found to be a multiple of the separation bubble size. The numerically estimated peak frequencies well conform with the previously introduced formula for swept supersonic interactions [Ceci *et al.*, J. Fluid Mech. **956**, R1 (2023)]. Proper orthogonal decomposition is applied to investigate the spatial structure of the corrugation at the separation point and educe phase relations between the flow structure and pressure oscillations at the reattachment point. The present analysis leads us to conclude that the same phenomenology found in swept supersonic interactions also holds in the hypersonic case.

DOI: 10.1103/PhysRevFluids.9.054603

I. INTRODUCTION

Recent years have been characterized by renewed interest in the design of hypersonic vehicles. The realization of a high-speed aircraft is associated, however, with enormous aerothermodynamic, propulsive, and structural challenges, which have hindered their operation [1]. However, the interest from commercial aircraft companies in drastically reducing the travel time in intercontinental flights, the continuous work operated by military organizations in introducing new aircraft concepts, and the deployment of new space activities have motivated additional effort on this topic by industries and researchers. Technical issues, developments, and perspectives on hypersonic flight were discussed in several review works over the past two decades [2–5].

As emphasized by Holden [6], accurate prediction of surface heating, wall pressure, and friction distributions is paramount for effective design of hypersonic vehicles. In this respect, shock wave/boundary layer interactions (SBLIs) can constitute a serious threat for the integrity of aircraft structures and have been the subject of intense research in the aerospace community [7–10]. Strong

---

[*] alessandro.ceci@uniroma1.it

adverse pressure gradients generated by a shock wave impinging on a boundary layer can be responsible for extensive flow separation associated with low-frequency pressure loads, mainly localized at the mean separation line. In addition, hypersonic SBLIs are characterized by intense wall heat transfer near reattachment, whose intensity depends on the shock strength [11–13]. Both phenomena pose serious concerns to high-speed vehicle design, as they can be responsible for structural and thermal fatigue.

The research on low-frequency pressure oscillations have mainly focused on “two-dimensional” interactions, in which the boundary layer direction is directed orthogonal to the shock impingement line. The analysis of two-dimensional configurations has revealed that “breathing” of the separation region [14] can be responsible for unsteadiness if strong separation is present. For mild separation, unsteadiness is ascribed to the alternation of high- or low-velocity streaky structures embedded in the approaching boundary layer [15].

Previous experimental, numerical, and theoretical studies have demonstrated the existence of those mechanisms in supersonic/hypersonic interactions and provided means for the development of physical models [14,16–18]. Modal decomposition techniques and mean flow-based stability analyses have been also applied to identify the main coherent structures in the interaction region for oblique shock reflections [19–21] and compression ramps [22–24]. Those approaches have allowed the identification of large-scale spanwise rippling of the separation line, which is coupled with corrugations and oscillatory motions of the reflected shock. For strong flow separation the typical frequency of those structures can be one order of magnitude less than those associated with the mixing layer and the turbulent motions, which also have smaller length scales.

However, in practical configurations the shock impingement line is rarely orthogonal to the flow main direction. In those cases, the separation/reattachment lines can be parallel as in two-dimensional cases (cylindrical symmetry) or departing from a virtual conical origin (conical symmetry). As observed by Settles *et al.* [25] and Erengil and Dolling [26], the type of interaction depends on the shock strength and the sweep angle. As widely discussed by the review article of Sabnis and Babinsky [27], canonical cases of three-dimensional SBLIs comprise flows over swept compression ramps [25,26,28–31], around single sharp fins [32–34], double fins [35,36], and oblique impinging shocks [37,38]. Most of the aforementioned studies do observe low-frequency oscillation of the pressure field around the separation shock foot, with characteristic frequencies generally higher than in two-dimensional interactions [10]. In fact, it is noteworthy that some studies [30] reported that the presence of large sweep inhibits low-frequency oscillations completely.

Most of the cited studies are based on experiments, with the only exception of the swept compression ramp simulations by Adler and Gaitonde [29,30] and Zhang *et al.* [31], and the large-eddy simulation (LES) of double-fin flow by Adler and Gaitonde [35]. Simulations of SBLI has been generally limited to simple cases, whose computational cost is affordable. A compromise solution to study three-dimensional interactions using high-fidelity simulations at moderate computational cost was considered by Gross and Fasel [39], Di Renzo *et al.* [40], Larsson *et al.* [41], Ceci *et al.* [42], and Bergier *et al.* [43]. In those works, a crossflow velocity is added to the incoming flow to emulate genuine three-dimensional effects. Their numerical setup allowed detection of changes in the mean flow topology and characterization of low-frequency oscillations as a function of the sweep angle. All those studies showed an increasing trend of the streamwise length of the mean separation region with the sweep angle. In addition, Ceci *et al.* [42] found evidence of spanwise ripples at mean separation, traveling along the interaction line at a fraction of the crossflow velocity. Those authors also found monotonic increase of the characteristic frequency of the pressure oscillations at the mean separation line with the sweep angle, as confirmed by Bergier *et al.* [43] via LES at higher Reynolds number.

The work by Ceci *et al.* [42] introduced a simple mechanistic model to explain and predict the changes in the low-frequency wall pressure spectrum, but this model was tested only at Mach 2.28. We think it is essential to test this (or indeed any) model at more than just a single Mach number. Given this background, extending current numerical results on supersonic swept SBLIs to the hypersonic regime would be of great importance. This study presents a data set of hypersonic

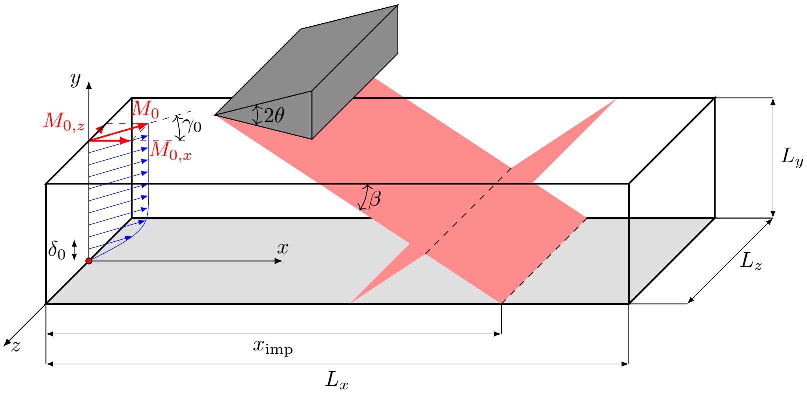

FIG. 1. Schematic of SSBLI: γ_0 is the incoming flow sweep angle; δ_0 is the incoming boundary layer thickness; β is the shock angle, θ the deflection angle, and x_{imp} the nominal location of the shock impingement.

impinging SBLI simulations with sweep, a flow condition that is not currently available in the literature to the best of our knowledge. Furthermore, the possibility of performing high-fidelity numerical simulations in hypersonic flow would also be attractive to gather information about the influence of sweep on heat transfer, which has been explored, to the authors' knowledge, by only one work in the supersonic regime [44]. Hence, we leverage the numerical data to analyze the effect of the sweep angle on the time-averaged flow properties, heat transfer, and low-frequency oscillations.

II. NUMERICAL METHODOLOGY

The analysis of the flow field generated by the unswept and swept interactions between an oblique shock and a turbulent boundary layer is carried out using the high-fidelity code STREAmS [45]. The working fluid is assumed to be an ideal gas, of heat capacity ratio $\gamma_g = 1.4$ and Newtonian law for viscous stresses. The dynamic viscosity of the mixture is evaluated using the power law $\mu = \mu_0(T/T_0)^{0.76}$, whereas the thermal conductivity λ_g is computed using a constant Prandtl number $\mathrm{Pr} = 0.72$.

The convective fluxes are discretized by means of a hybrid scheme which combines the energy-preserving properties of a sixth-order skew-symmetric central difference scheme [46] with the shock-capturing properties of a fifth-order weighted essentially nonoscillatory (WENO) scheme. The switch between the two methods is controlled by a modified Ducros sensor

$$\Theta = \frac{-\boldsymbol{\nabla}\cdot\mathbf{u}}{\sqrt{(\boldsymbol{\nabla}\cdot\mathbf{u})^2 + (\boldsymbol{\nabla}\times\mathbf{u})^2 + (u_0/\delta_0)^2}}, \tag{1}$$

which is activated when $\Theta > 0.25$ for any of the points belonging to the WENO stencil. The diffusive fluxes, expanded to Laplacian form, are discretized with sixth-order central formulas, and the time advancement is carried out with a third-order Runge-Kutta scheme [47]. The main elements of the numerical setup are sketched in Fig. 1. A turbulent boundary layer with thickness δ_0 is injected at the left boundary of the computational domain ($x/\delta_0 = 0$), being swept by an angle γ_0 with respect to the positive x direction. The instantaneous velocity at the inflow is obtained as the sum of an inverse Van Driest transform of Musker family incompressible mean turbulent profiles and fluctuations obtained using recycling-rescaling with spanwise shift [48]. The temperature fluctuation field is in turn obtained from the streamwise velocity one using the strong Reynolds analogy. The flat plate is assumed to be isothermal and slightly cooled, with the wall-to-recovery temperature ratio set to $T_w/T_r = 0.8$. An oblique shock impinges the flat plate orthogonal to the x direction, at $x_{\text{imp}} = 64\delta_0$. The shock is introduced into the numerical domain by hard enforcement of the Rankine-Hugoniot jump relations on the top boundary. Periodicity of the flow is assumed in the z direction, and nonreflecting boundary conditions are instead imposed at the top and outlet boundaries.

The discretization of the computational domain is based an on uniform grid spacing along the x and z directions. A stretching transformation, proposed by Ceci and Pirozzoli [49], is used in the y direction, which accounts for the local distribution of the Kolmogorov length scale η in compressible wall-bounded flows. A maximum resolution threshold of $\Delta y/\eta \approx 2.5$ for all cases and a minimum spacing of $\Delta y_w^+ = \Delta y_w/\delta_v = 0.5$ at the wall are considered to define the wall-normal grid distribution, with the only exception of the finest grid simulation (case G00_T14F), used for grid independence purposes.

The set of numerical simulations is summarized in Table I. Three different values of the sweep angle γ_0 are considered, namely, $\gamma_0 = \{0, 15, 30\}^\circ$. The unswept case will be denoted as "baseline." The same projected Mach number along the streamwise direction ($M_{0,x} = 5$) is used in all computations, thereby obtaining different values of M_0 for the swept cases. All computations roughly share the same value of Re_{δ_2} at a reference location of $x_r = 45\delta_0$, just upstream of the interaction region. The shock deflection angle is kept constant to $\theta = 14^\circ$ for all computations. The chosen Mach number, wall temperature ratio, and shock deflection angle of the unswept case are chosen to match that of the strongest shock case investigated by Schülein [50] using experimental techniques, and more recently through numerical simulations by Volpiani *et al.* [11] and Yu *et al.* [13].

The numerical domain is constituted by a box whose dimensions $L_x \times L_y \times L_z = 100\delta_0 \times 10\delta_0 \times 50\delta_0$. The numerical grid is composed of $3200 \times 480 \times 1600$ grid points along the x, y, and z directions. The corresponding wall spacings, evaluated at the reference position, are $\Delta x^+ = \Delta z^+ = 6.9$.

The combined effect of grid resolution and domain width of mean flow properties, as the wall friction coefficient and heat transfer, is assessed for the baseline case by two additional computations. A simulation with the same grid spacing as the baseline (case G00_T14N) is used to investigate the effect of the spanwise domain width on the resulting flow properties. A finer grid simulation (case G00_T14F), whose spanwise domain extension is sharply reduced to $L_z = 5\delta_0$, whereas the node density in the x and z direction is doubled, is used to infer dependence from mesh spacing. It must be expected, based on previous analysis in the supersonic case [42], that negligible dependence of the mean flow properties on the domain spanwise width is obtained by changing L_z at constant grid resolution.

The turbulence statistics are evaluated by averaging over a $2200\,\delta_0/u_0$ time window for all cases, with exception of the most refined case, whose averages are evaluated over a time span of $1100\,\delta_0/u_0$. Spanwise averaging is also performed as after flow homogeneity. The accumulation of the statistics is started after a statistically steady state condition is reached, as estimated by monitoring the spanwise-averaged location of the separation point. Snapshots of wall pressure are collected at a constant sampling rate $\Delta t_s u_{0,x}/\delta_0 = 0.237$ and used for spectral analysis and modal decomposition. The computed spectra are obtained by applying the Welch method to the pressure signal, using three segments with 50% overlap and Hamming windowing. The same samples are used also for the proper orthogonal decomposition (POD) analysis, which we carry out following the original approach of Sirovich [51].

The validity of the present setup is assessed by comparing the time-averaged flow properties of the unswept cases (G00_T14 and its variants G00_T14F and G00_T14N of Table I) against previous literature results, and by carrying out domain/mesh independence studies. In this respect, experimental measurements by Schülein [50] and numerical data by Volpiani *et al.* [11] serve as concurrent validation data sets.

Figure 2 reports the streamwise evolution of the mean wall pressure scaled by the freestream value and the local friction coefficient ($c_f = 2\tau_w/(\rho_0 u_0^2)$). For all data sets, the x axis is scaled using the conventional boundary layer thickness at the inviscid shock location (δ_{imp}).

Overall, we find fairly good agreement between the present numerical setup and previous simulations. The extent of the interaction region is in line with what was found by Volpiani *et al.* [11], both

TABLE I. Summary of the numerical simulations. $M_{0,x}$ is the x-projected Mach number, M_0 the freestream Mach number, γ_0 the sweep angle, $\mathrm{Re}_{\delta_0} = \rho_0 u_0 \delta_0/\mu_w$ the boundary layer thickness based Reynolds number at the inflow location, N_x, N_y, N_z the total number of grid points along the x, y, and z directions, L_x, L_y, L_z the domain size, and Δx^+, Δy_w^+, Δz^+ the streamwise, wall normal (near-wall), and spanwise resolutions.

Label	$M_{0,x}$	M_0	γ_0	$\theta(^\circ)$	Re_{δ_0}	$N_x \times N_y \times N_z$	$(L_x \times L_y \times L_z)/\delta_0$	$\Delta x^+ \times \Delta y_w^+ \times \Delta z^+$	Line color
G00_T14	5	5	0	14	55 474	$3200 \times 480 \times 1600$	$100 \times 10 \times 50$	$6.9 \times 0.5 \times 6.9$	🟥
G15_T14	5	5.18	15	14	58 146	$3200 \times 480 \times 1600$	$100 \times 10 \times 50$	$6.9 \times 0.5 \times 6.9$	🟩
G30_T14	5	5.77	30	14	75 132	$3200 \times 480 \times 1600$	$100 \times 10 \times 50$	$6.9 \times 0.5 \times 6.9$	🟦
G00_T14F	5	5	0	14	55 474	$6400 \times 528 \times 320$	$100 \times 10 \times 5$	$3.4 \times 0.3 \times 3.4$	🟥
G00_T14N	5	5	0	14	55 474	$3200 \times 480 \times 160$	$100 \times 10 \times 5$	$6.9 \times 0.5 \times 6.9$	⬛

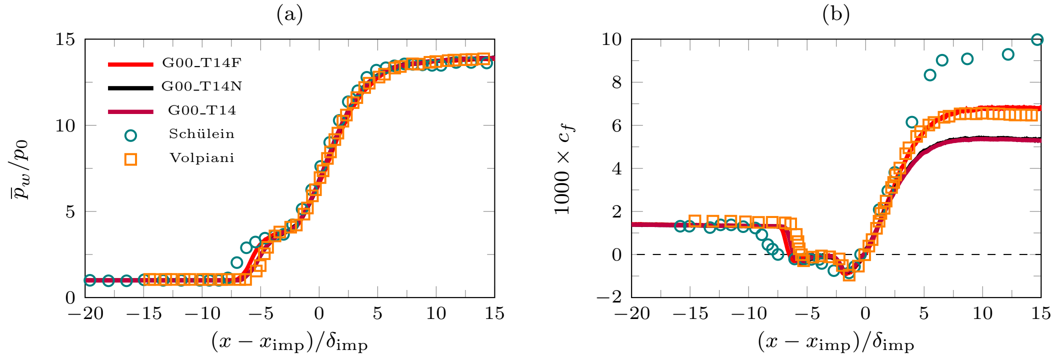

FIG. 2. Numerical validation: streamwise distributions of time-averaged wall pressure (a) and friction coefficient (b). Solid lines denote the results of the present numerical simulations (red line: case G00_T14F; purple line: case G00_T14; black line: case G00_T14N), orange symbols denote numerical data [11], and dark green symbols denote experimental data [50].

being smaller than the experimental one. It must be noted that Schülein [50] reported experimental uncertainties in the skin friction ranging between 4% and 10%, the latter being detected for the peak of shear stress near the reattachment point. Hence, the discrepancy between experimental and numerical results cannot be attributed to measurement errors, whereas three-dimensional effects in the experimental setup can play a major role in that regard. In addition, the finest simulations predict similar distributions of the friction coefficient past reattachment, although much smaller than the experimental one. In this case, differences between numerical and experimental data are likely due to insufficient mesh resolution in the relaxation region, due to the sharp drop of the viscous length scale ($\delta_v = \mu_w/\sqrt{\rho_w \tau_w}$) in the region after reattachment, since both ρ_w and τ_w increase.

This hypothesis can be easily tested by inspecting the c_f behavior between the coarser grid and the finest one of the present set of simulations. We thus expect the friction coefficient in the relaxation region to further rise as the grid resolution is improved. The behavior of the inner-scaled mesh size along the streamwise direction for the present set of simulations is reported in Fig. 3. In this context, it can be stated that the current work features a DNS-level resolution before the interaction region and transitions to a resolution similar to LES after the impingement location. It is clear that carrying out a full DNS-based parametric study of hypersonic SBLI including the relaxation zones would require an enormous amount of computer resources, and it will be the subject

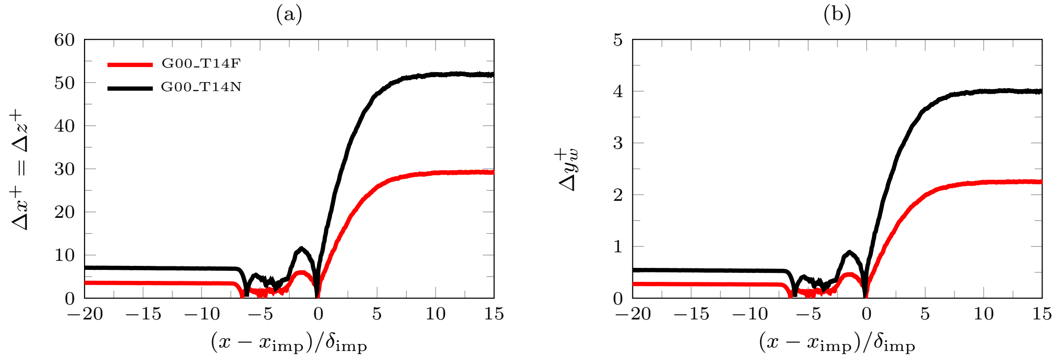

FIG. 3. Streamwise distribution of the inner-scaled mesh sizes for the baseline simulation in narrow domain G00_T14N (black lines) and for the finer one G00_T14F (red lines): $\Delta x^+ = \Delta z^+$ (a), Δy_w^+ (b).

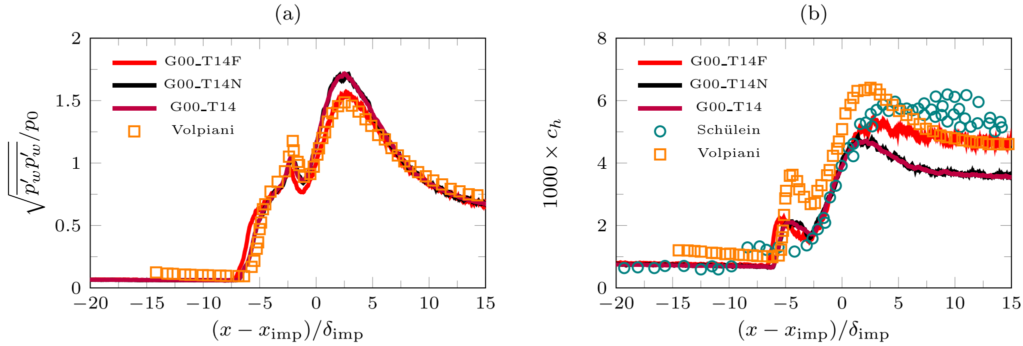

FIG. 4. Numerical validation: streamwise profiles of the nondimensional wall pressure r.m.s. [$\sqrt{\overline{p'_w p'_w}}/p_0$, (a)] and Stanton number [$c_h = q_w/[\rho_0 u_0 c_p (T_w - T_r)]$, (b)]. Solid lines denote the results of the present numerical simulations (red line: case G00_T14F; purple line: case G00_T14; black line: case G00_T14N), the orange symbols denote numerical data [11], and the dark green symbols denote experimental data [50].

of future research. However, the baseline and finer grid results for the time-averaged wall pressure, friction coefficient, wall pressure fluctuations, and heat transfer coefficient (Figs. 2 and 4) collapse all the way up to 2.5 δ_{imp} past reattachment. We therefore deem the results from the baseline grid fully reliable in that region.

Figure 4 shows the streamwise profiles of the pressure fluctuations intensity and of the Stanton number, defined as

$$c_h = \frac{q_w}{\rho_0 u_0 c_p (T_w - T_r)}, \tag{2}$$

where q_w is the local heat flux. It is worth noting that the velocity scale in this definition is $u_0 = u_{0,x}/\cos(\gamma_0)$, in compliance with the definition of the recovery temperature. The analysis of the pressure fluctuation distributions yields similar conclusion as the previous ones. The fine grid simulation well conforms with the previous numerical simulations, whereas a spurious overshoot is found on the coarsest mesh. Different conclusions hold for the Stanton number, namely, the present results are in good agreement with the experimental data, at least up to the reattachment point. Abnormally high values of the Stanton number are instead retrieved in the numerical simulations of Volpiani *et al.* [11], also in the incoming boundary layer. In this case, Schülein [50] reported repeatability errors of ±5% for heat flux measurements, which makes the prediction of the present fine grid simulation quite reliable.

It is noteworthy that the effect of increasing the domain width at a fixed mesh resolution is negligible, as expected by previous simulations in the supersonic regime [42]. Finally, we show the achievement of a fully developed turbulence state upstream of the interaction region by inspecting the Van Driest transformed mean velocity, defined as

$$u_{VD} = \int_0^u \sqrt{\overline{\rho}^+} du, \tag{3}$$

and the Reynolds stresses profiles. Figure 5(a) depicts the inner-scaled mean velocity profiles from different sources [11,50,52]. Good agreement is obtained with respect to the reference incompressible distribution throughout the wall layer. Small effects of insufficient grid spacing are found when comparing the profiles of cases G00_T14 and G00_T14F, with differences which, however, do not exceed 2% in the logarithmic region. Figure 5(b) instead shows close agreement between the distributions of the Reynolds stresses from the finest G00_T14F simulation, and the data set of Volpiani *et al.* [11], and largest differences between the baseline and fine grid stresses of about 3%, for the peak streamwise velocity variance.

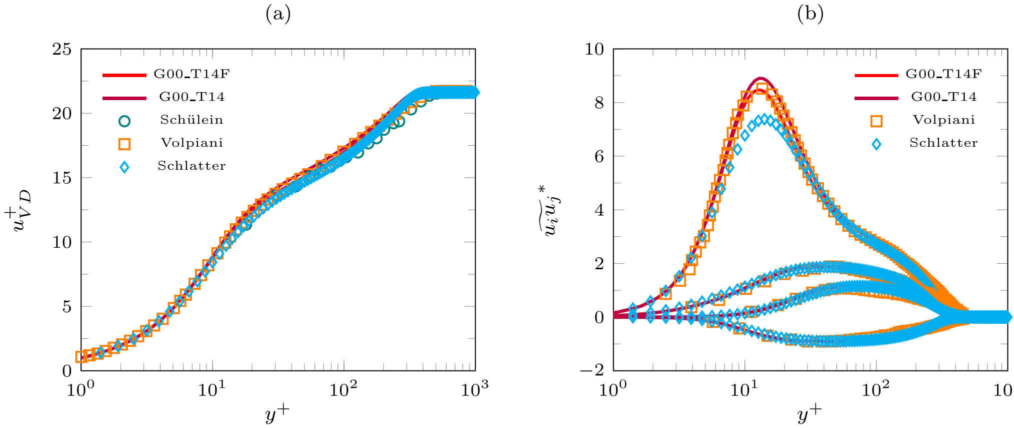

FIG. 5. Wall-normal profiles of Van Driest transformed, Favre-averaged streamwise velocity profiles $\tilde{u}^+_{VD}$ (left) and density-scaled stresses $\widetilde{u_i u_j}^* = \overline{\rho u_i'' u_j''}/\tau_w$ (right) for different data sets at $x_r = 45\delta_0$: baseline G00_T14 (purple solid line), finer mesh G00_T14F (red solid line), Volpiani *et al.* [11] (orange squares), Schlatter and Örlü [52] (cyan diamonds), and experiments of Schülein [50] (dark green circles).

III. MEAN FLOW PROPERTIES

A. Incoming boundary layer

A first step in the assessment of the flow conditions in the incoming boundary layer includes checking the distribution of the inner-scaled velocity at the upstream reference station. Figure 6(a) compares the Favre-averaged velocity profiles in the swept direction $\tilde{u}_s = \sqrt{\tilde{u}^2 + \tilde{w}^2}$, obtained from the G00_T14, G15_T14, and G30_T30 flow cases. Under the Van Driest transformation all curves collapse, which is not surprising as $\mathrm{Re}_{\delta,2} = 1250$ is held the same for all simulations.

It is important to note that when crossflow is added to the main stream, the effective Mach number increases as $M_0 = M_{0,x}/\cos(\gamma_0)$, hence the recovery temperature increases as well, giving rise to different density and temperature distributions across the boundary layer. In Fig. 7 we show the

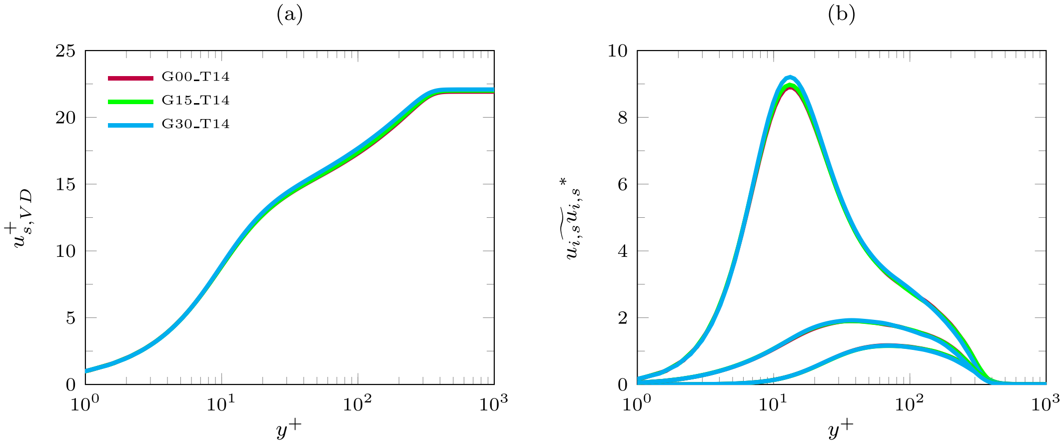

FIG. 6. Wall-normal profiles of Van Driest transformed, Favre-averaged velocity profiles $\tilde{u}^+_{s,VD}$ (a) and density-scaled stresses $\widetilde{u_{i,s} u_{i,s}}^* = \overline{\rho u_{i,s}'' u_{i,s}''}/\tau_w$ (b) for different sweep angle, at the reference position $x_r = 45\delta_0$. Unswept case (purple line), swept case with $\gamma_0 = 15^\circ$ (green line); swept case with $\gamma_0 = 30^\circ$ (cyan line). The subscript s denotes quantities along the freestream direction.

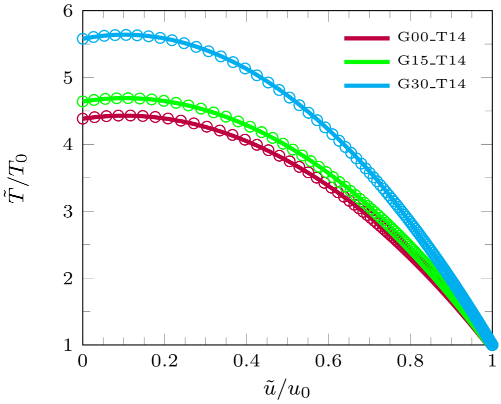

FIG. 7. Temperature-velocity relation for the unswept interaction (solid purple line), swept case with $\gamma_0 = 15^\circ$ (solid green line), and swept case with $\gamma_0 = 30^\circ$ (solid blue line) at $x_r = 45\delta_0$. The hollow circles denote the relation proposed by Duan *et al.* [53].

velocity-temperature relation for the three cases under scrutiny. Excellent prediction of the profiles is obtained by applying the relation of Duan *et al.* [53].

B. Interaction region

Figure 8(a) shows the distribution of the mean wall pressure across the interaction zone. Earlier upstream influence is observed in the swept cases, with the largest interaction region exhibiting a narrow pressure plateau from $-5 \leqslant (x - x_{\text{imp}})/\delta_{\text{imp}} \leqslant -2$. This well conforms with the distribution of the mean streamwise-projected friction coefficient, shown in Fig. 8(b), which displays earlier separation and retarded reattachment for cases with crossflow. The effect of the sweep angle on the separation length is clearly nonlinear. Sharp increase of the wall friction is observed past reattachment, leading to very small value of the viscous length scale. The locations of the mean separation x_{sep} and reattachment points x_{rea}, as well as the separation length $L_{\text{sep}} = x_{\text{rea}} - x_{\text{sep}}$ are listed in Table II for all three cases.

Figure 9 depicts the distributions of the wall pressure r.m.s. and of the Stanton number. A similar pattern of the pressure fluctuations is retrieved in all cases, with peaks within the separation zone

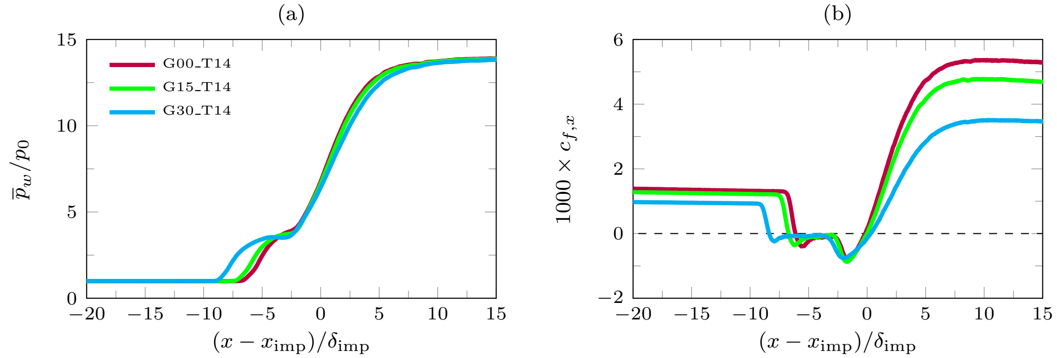
(a)

(b)

FIG. 8. Streamwise distribution of mean wall pressure (a) and x-projected friction coefficient ($c_{f,x} = 2\mu_w(\text{du}/\text{dy})|_{\text{w}}/(\rho_0 \text{u}_0^2)$, (b)). Unswept case (purple line), swept case with $\gamma_0 = 15^\circ$ (green line), and swept case with $\gamma_0 = 30^\circ$ (blue line).

TABLE II. Location of mean separation and reattachment points and mean separation length for the swept and unswept SBLIs.

Label	$\gamma_0(^\circ)$	$(x_{\mathrm{sep}} - x_{\mathrm{imp}})/\delta_{imp}$	$(x_{\mathrm{rea}} - x_{\mathrm{imp}})/\delta_{\mathrm{imp}}$	$L_{\mathrm{sep}}/\delta_{\mathrm{imp}}$
G00_T14	0	−6.15	−0.15	6.0
G15_T14	15	−6.71	−0.01	6.7
G30_T14	30	−8.37	0.28	8.6

and past reattachment, and flattening at the highest crossflow angle. A double-peak structure is also found in the Stanton number, which shows large values in the interaction region and past reattachment. The fact that the peak heat flux is lower in swept cases for fixed pressure ratio is a nontrivial result, which cannot be predicted from standard correlations for two-dimensional SBLI [11,13].

Figure 10 illustrates contour plots of the mean streamwise velocity in the x-y plane, for $\gamma_0 = 0^\circ, 15^\circ, 30^\circ$. It is evident that the size of the separation bubble increases as γ_0 increases, which results in upstream shift of the virtual origin of the reflected shock. The whole system of impinging, reflected, and reattachment shocks is clearly visible in all cases under scrutiny, with the mean reflected and reattachment shocks, which are significantly bent in the outer potential flow region and eventually coalesce into a single shock.

Visualisations of streamlines and friction lines are given in Fig. 11, in which the dividing streamline is determined by integrating $\partial\psi/\partial y = \overline{\rho u}$ in the wall-normal direction. As the flow is three-dimensional, the maps in Fig. 11 are obtained by projecting the velocity vectors onto the dividing streamline. As expected, all stream traces are aligned along the nominal free-stream direction upstream of the interaction zone. The flow pattern in the separated region is more complex in swept interactions, in which the flow becomes basically aligned along the spanwise direction in regions where wall friction is negative but very close to zero. In the relaxation region, the flow tends to follow the direction of the postshock inviscid state, with spanwise velocity being unchanged, and reduced streamwise velocity. The strongest deviations occur within the interaction zone, in which the stream traces are deflected upwards and decelerated along the streamwise direction, while keeping the same spanwise velocity. Hence, the flow is still pointing along the positive-x direction, but the streamlines are more skewed than the approaching boundary layer.

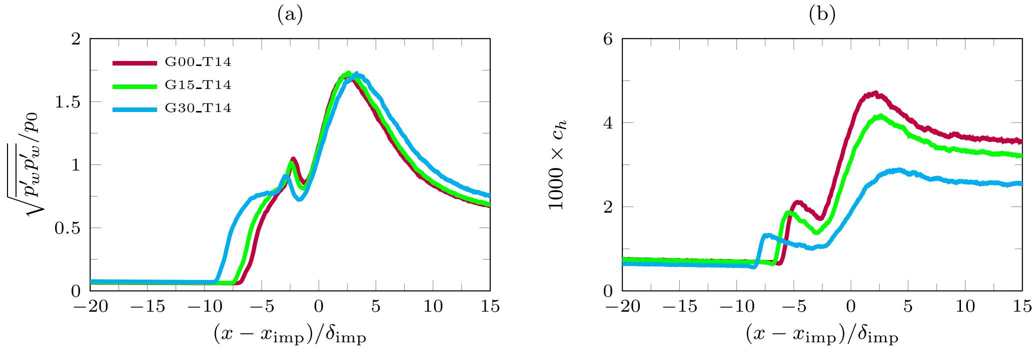

FIG. 9. Streamwise distribution of time-averaged of wall pressure root-mean square $\sqrt{\overline{p'_w p'_w}}/p_0$ and Stanton number c_h. Unswept case (purple line), swept case with $\gamma_0 = 15^\circ$ (green line), and swept case with $\gamma_0 = 30^\circ$ (cyan line).

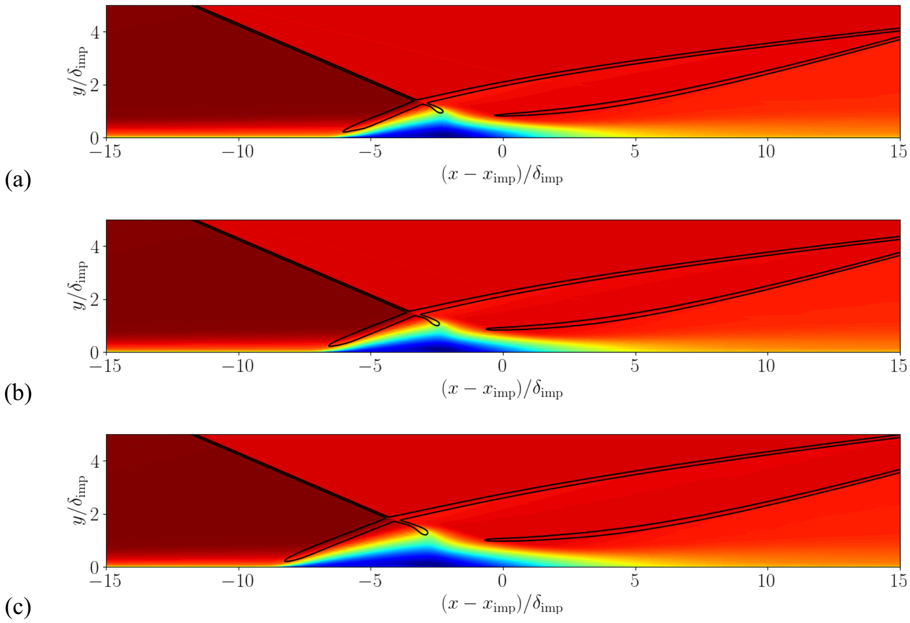

FIG. 10. Mean streamwise velocity field (u) at various crossflow angles, for $T_w/T_r = 0.8$. Contour levels are shown in the range $0 < u/u_{0,x} < 1$; (a) $\gamma_0 = 0^\circ$, (b) $\gamma_0 = 15^\circ$, and (c) $\gamma_0 = 30^\circ$. A mean dilatation isoline (in black) is used to highlight the shock system.

The mean flow distortion due to the reflected-impinging shock system is quantified in terms of the mean flow direction angles, namely,

$$\gamma_w = \tan^{-1}\left(\frac{\tau_{xz}}{\tau_{xy}}\right), \quad \gamma_s = \tan^{-1}\left(\frac{\widetilde{w}}{\widetilde{u}}\right), \tag{4}$$

respectively at the wall and for a generic streamline, whose distributions are reported in Fig. 12. Consistent with previous results reported in Fig. 11 and with previous studies in supersonic conditions [40,43], we find $\gamma_w > 90^\circ$ within the interaction region, which corresponds to time-averaged reversed motion with respect to the x direction. The strength of the reverse flow and flow distortion along the dividing streamline are seen to reduce as the sweep angle is increased. In all cases the values of γ_w and γ_s in the relaxation region slowly approach the inviscid value. Close inspection of Figs. 11 and 12, reveals that the mean flow behavior of the fluid particles sufficiently far from the wall consists of uplift and downlift, respectively, at the onset and the end of the separation region, accompanied by spanwise displacement. Likewise, a particle close to the wall travels from the reattachment line in a reversed direction, with a crossflow velocity much larger than the streamwise. The angle between the mean velocity vector and the spanwise direction appears to be equal and opposite for particles traveling near the wall and along the dividing streamline towards the edges of the separation bubble, whereas the behavior in the central part is largely different.

C. Scrutiny of free-interaction theory

The observation that the interacting flow upstream of the separation bubble depends neither on the source of separation nor on the downstream geometry led Chapman *et al.* [54] to propose that supersonic flow separation is a local self-induced, free-interaction process between the boundary layer and the outer inviscid stream [8,54–56]. The starting point is the mean momentum balance at

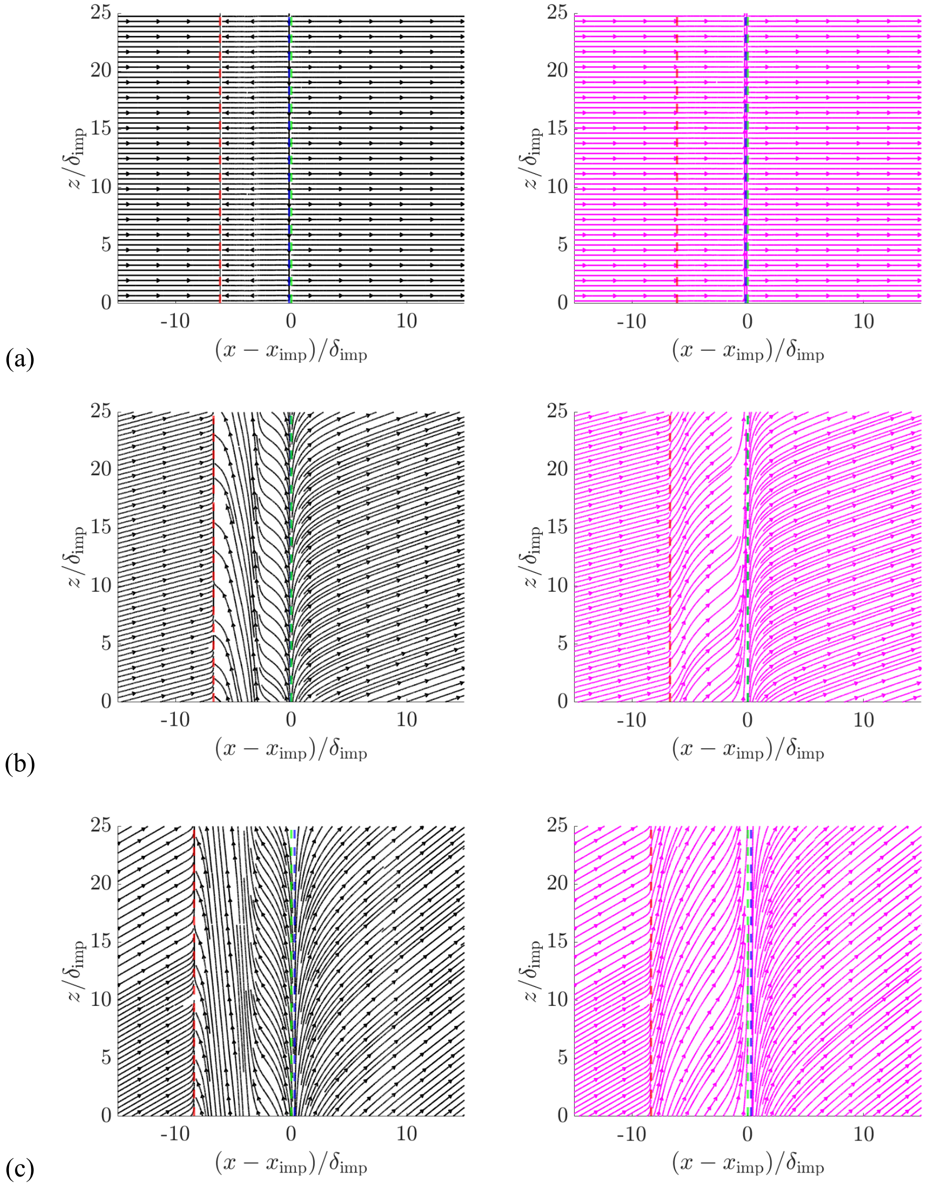

FIG. 11. Mean friction lines at the wall (left) and mean streamlines along the dividing streamline (right), for (a) $\gamma_0 = 0^\circ$, (b) $\gamma_0 = 15^\circ$, and (c) $\gamma_0 = 30^\circ$. The mean separation lines are shown in red, the shock impingement lines in green, and the reattachment lines in blue.

the wall, which yields

$$0 = -\frac{\mathrm{d}\overline{p}}{\mathrm{d}x}\Big|_w + \frac{\partial \tau}{\partial y}\Big|_w . \tag{5}$$

Integration of this equation from the origin of the interaction (x_i) to a generic x location yields

$$\frac{\overline{p}(s) - p_0}{q_0} = c_{f,i}\frac{L^*}{\delta_i^*}\int_0^s \frac{\partial \tau_w/\tau_{w,i}}{\partial y/\delta_i^*}\Big|_w \mathrm{d}s = c_{f,i}\frac{L^*}{\delta_i^*} f_1(s), \tag{6}$$

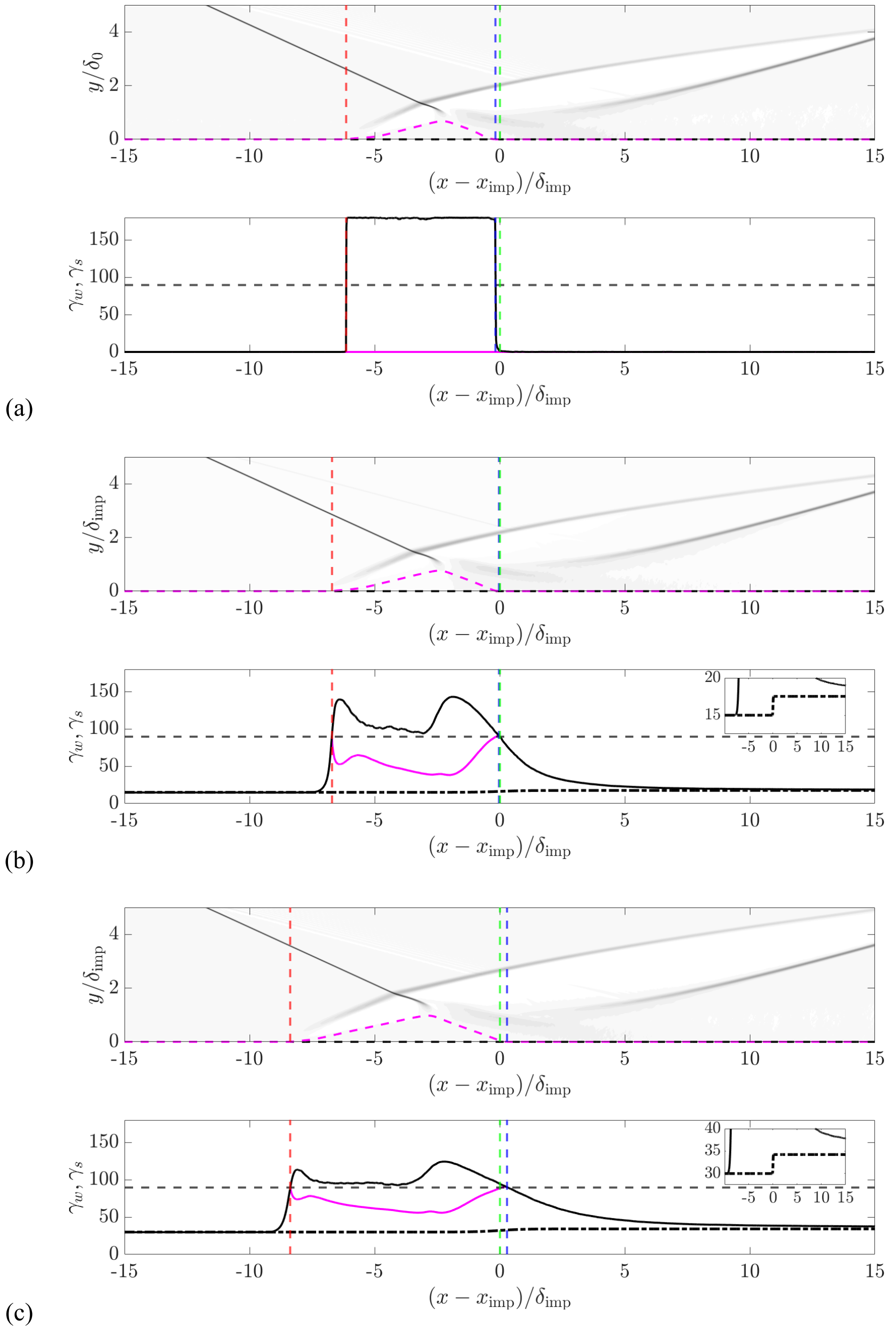

FIG. 12. Numerical schlieren visualization based on the streamwise density gradient (top), and streamwise evolution of flow angles (bottom), for (a) $\gamma_0 = 0^\circ$, (b) $\gamma_0 = 15^\circ$, and (c) $\gamma_0 = 30^\circ$. The magenta dashed lines refer to the shape of the dividing streamline, and the magenta solid lines refer to the corresponding flow angle in the wall plane, the black dashed lines refer to the wall surface, and the black solid line to the wall-parallel friction lines. Dashed red, green, and blue lines denote the mean separation, impingement and reattachment positions, respectively.

where $s = (x - x_i)/L^*$, with L^* a suitable interaction length scale, and where

$$c_{f,i} = \frac{\tau_{w,i}}{q_0}, \quad q_0 = \frac{1}{2}\rho_0 u_0^2, \tag{7}$$

are evaluated on the control point x_i, located just upstream of the interaction. Hereafter, the subscript $(\cdot)_i$ denotes boundary layer properties taken at this position, while inviscid quantities as Mach number, pressure, and dynamic pressure at x_i are assumed to be identical to the inflow state, denoted by the subscript $(\cdot)_0$. In Eq. (6) we assume that the pressure rise follows a similarity law, defined as $f_1(s)$, in terms of the streamwise coordinate s.

Another equation is needed to connect the boundary layer thickening and pressure variations in the outer inviscid flow. As reported in previous studies of two-dimensional SBLIs [8,54,57], a link between the flow deflection φ and the pressure variation $\Delta\overline{p} = \overline{p} - p_0$ is obtained from the assumption of linearized simple-wave flow

$$\frac{\sqrt{M_0^2 - 1}}{\gamma_g M_0^2}\frac{\Delta\overline{p}}{p_0} - \Delta\varphi = 0, \tag{8}$$

where $\Delta\varphi = \varphi - \varphi_i = \varphi$ denotes the difference in the local flow deflection angle from its upstream value φ_i, which can reasonably be neglected as x_i is located upstream of the interaction region. It is worth mentioning that Eq. (8) governs the evolution of an isentropic flow under small compression and expansion. The flow deflection is determined from the boundary layer displacement thickness,

$$\varphi = \tan^{-1}\left(\frac{\mathrm{d}\delta^*}{\mathrm{d}x}\right) \approx \frac{\mathrm{d}\delta^*}{\mathrm{d}x}. \tag{9}$$

By introducing scaled quantities, the above equation becomes

$$\varphi = \frac{\delta_i^*}{L^*}\frac{\mathrm{d}\delta^*/\delta_i^*}{\mathrm{d}s} = \frac{\delta_i^*}{L}f_2(s), \tag{10}$$

where $f_2(s)$ is a universal function, and Eq. (8) becomes

$$\frac{\overline{p}(s) - p_0}{q_0} = \frac{2}{\sqrt{M_0^2 - 1}}\frac{\delta_i^*}{L}f_2(s). \tag{11}$$

Taking the product of Eq. (6) and Eq. (11), the pressure rise across the interaction zone is obtained as

$$\frac{\overline{p}(s) - p_0}{q_0} = F(s)\sqrt{\frac{2c_{f,i}}{\left(M_0^2 - 1\right)^{1/2}}}, \tag{12}$$

where

$$F(s) = \sqrt{f_1(s)f_2(s)}. \tag{13}$$

It is noteworthy that in Eq. (12), the origin of the interaction and its characteristic length scales are not specified. We then use simulation data to determine which choice of the two parameters yields the greatest degree of universality. The distributions of the similarity function determined from Eq. (12) are shown in Fig. 13, in which we take the origin of the free-interaction zone to be, respectively, the mean separation point (x_{sep}) and the point where the wall pressure gradient is maximum (x_p). In each panel we also consider different reference length scales, namely, the incoming boundary layer thickness (δ_i) and the distance between the location where $F = 4.22$ (x_m) and the origin [57,58]. The latter choice is frequently used in experiments as a surrogate for the separation point location. Inspection of our simulation data has instead shown (not reported) that such a value is attained close to the virtual origin of the separation bubble [41]. The data are presented along with results for supersonic swept interactions [42]. Figures 13(a) and 13(b) show

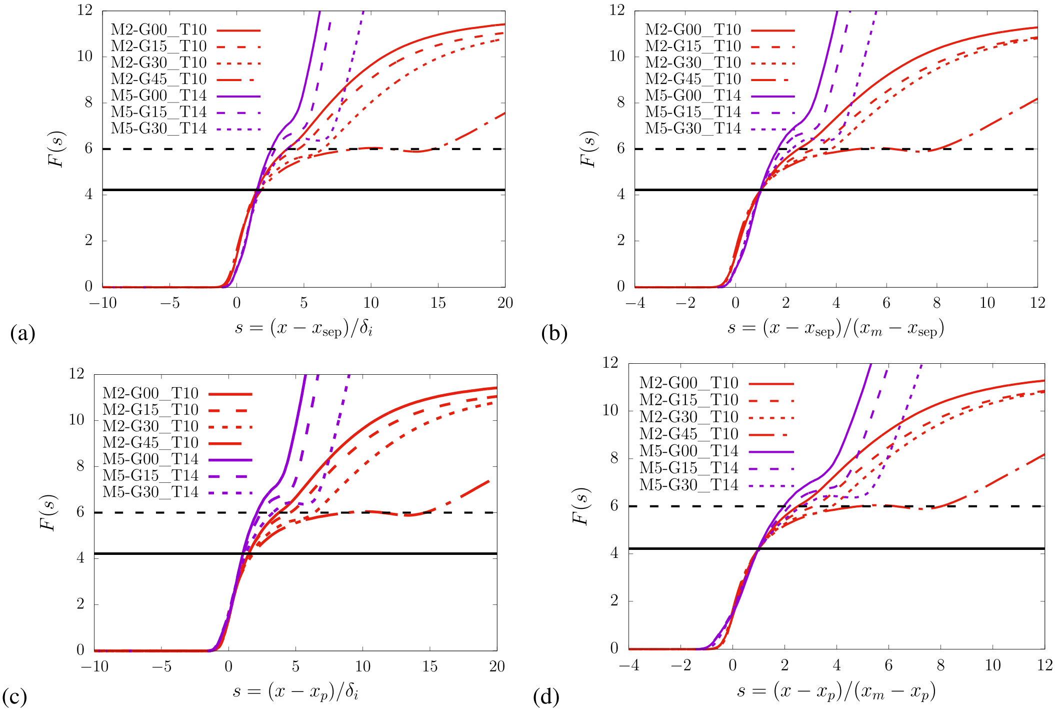

FIG. 13. Similarity function $F(s)$, as defined in Eq. (12), plotted by setting the origin (x_i) at the mean separation point (x_{sep}, panels a, b), and at the location of maximum pressure gradient (x_p, panels c, d). The reference length is taken to be either $L^* = \delta_i$ (a, c), or as the distance of the point where $F = 4.22$ (x_m) from the origin (b), (d).

that, if the separation point is used as the origin, $F(0) \approx 1$ for hypersonic cases, and $F(0) \approx 1.6$ for the supersonic cases, in agreement with the results of Volpiani *et al.* [11] and Matheis and Hickel [57]. More generally, good collapse is observed, separately for supersonic and hypersonic cases, up to $F_s = 4.22$. The various curves tend to show much larger scatter further downstream, and a genuine plateau is only observed for $M_0 = 2$, $\gamma_0 = 45^\circ$, with value of $F \approx 6$, in agreement with reference experimental data [59]. This is consistent with the established notion that the formation of a plateau requires extensive separation.

When the maximum pressure gradient location is used instead (panels c, d), universality between supersonic and hypersonic cases improves significantly, with $F \approx 1.6$ at the separation point, for all cases. Furthermore, all distributions virtually collapse in the initial part of the interaction when $L^* = \delta_i$, which indicates that the incoming boundary layer state is important in the early stages of the boundary layer separation process. Farther downstream, large scatter is still observed, although the choice $L^* = x_m - x_i$ yields greater universality of the distributions.

IV. LOW-FREQUENCY DYNAMICS

A spectral analysis is herein carried out to characterize unsteady processes in the interaction zone. For reference, in Table III we report the minimum resolved frequency and the peak frequency for all the flow cases. Preliminary examination of the spectra for the G00_T14 flow case was carried out, by applying the Welch method with three, five, or seven segments. The results displayed in Fig. 14 show that the signal-to-noise ratio is greatly reduced when three segments are used instead of a

TABLE III. Minimum resolved and peak frequency of the large scale unsteadiness expressed in term of St_L.

Label	$\mathrm{St}_{L,\min}$	$\mathrm{St}_{L,\mathrm{peak}}$
G00_T14	0.00763	0.0534
G15_T14	0.0114	0.114
G30_T14	0.0153	0.275

single segment, while still maintaining sufficient frequency resolution to resolve the low-frequency dynamics.

Maps of the normalized power spectral density (PSD) of wall pressure $\hat{E}_p(f) = E_p(f)/\int E_p(f)\,\mathrm{d}f$, are shown in Fig. 15, in premultiplied form, for two-dimensional and swept interactions. Consistent with previous scaling laws [14,16], the unswept case in Fig. 15(a) shows the occurrence of low-frequency dynamics at $10^{-2} \leqslant \mathrm{St}_{L,0} \leqslant 10^{-1}$ ($\mathrm{St}_L = fL_{\mathrm{sep}}/u_{0,x}$ is the Strouhal number based on the separation length and $\mathrm{St}_{L,0}$ its baseline value), with the peak occurring at $\mathrm{St}_{L,0} = 0.0534$, in a narrow region around the mean separation point. Numerical results of swept cases show instead substantial increase of the peak frequency, with $10^{-1} \leqslant \mathrm{St}_L \leqslant 10^0$. More precisely, the peaks occur at $\mathrm{St}_L = 0.114$ and $\mathrm{St}_L = 0.275$, for cases G15_T14 and G30_T14, respectively.

The spanwise PSD of pressure fluctuations at the mean separation line, $\hat{E}_p(\kappa_z) = E_p(\kappa_z)/\int E_p(\kappa_z)\,\mathrm{d}\kappa_z$, is shown in Fig. 16 to quantitatively characterize the rippling of the separation line. Good collapse of all PSD distributions in the high-wavelength end is achieved if the length of the separation bubble is used for normalization. In all cases, two spectral peaks are present, one at small wavelength ($\lambda_z \approx 0.1L_{\mathrm{sep}}$), which would probably correspond to the small-scale rippling noticed in previous numerical simulations of nonswept SBLI [19]. However, the most prominent peak is found to reside at much longer wavelengths ($\lambda_z \approx 2L_{\mathrm{sep}}$), which is linked to the presence of large-scale corrugations. As a consequence, observation of such peak requires use of wider domains than typically used in DNS, and accurate resolution of the peak wavenumber would require extremely large domains.

The previous results provide solid evidence that the same phenomena found in supersonic swept interaction also persist in hypersonic cases. In fact, large-scale rippling is still apparent near the separation point, with characteristic wavelength $2L_{\mathrm{sep}}$, irrespective of the sweep angle. Wave-number–frequency spectra at the separation line are then considered in Fig. 17 to characterize the advection velocity of those pressure disturbances. This quantity is evaluated following Choi and Moin [60]: for the ith time segment, the fluctuating wall pressure signal along the separation line

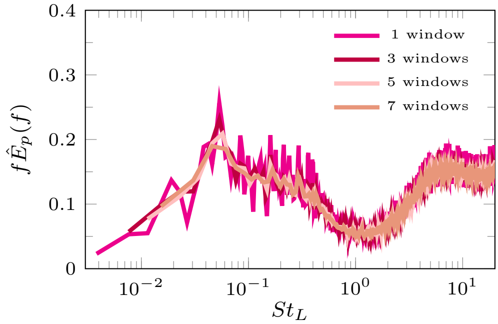

FIG. 14. Premultiplied, normalized PSD of wall pressure for the baseline flow case G00_T14, determined from use of the Welch method with one, three, five, and seven Hamming windows with 50% overlap.

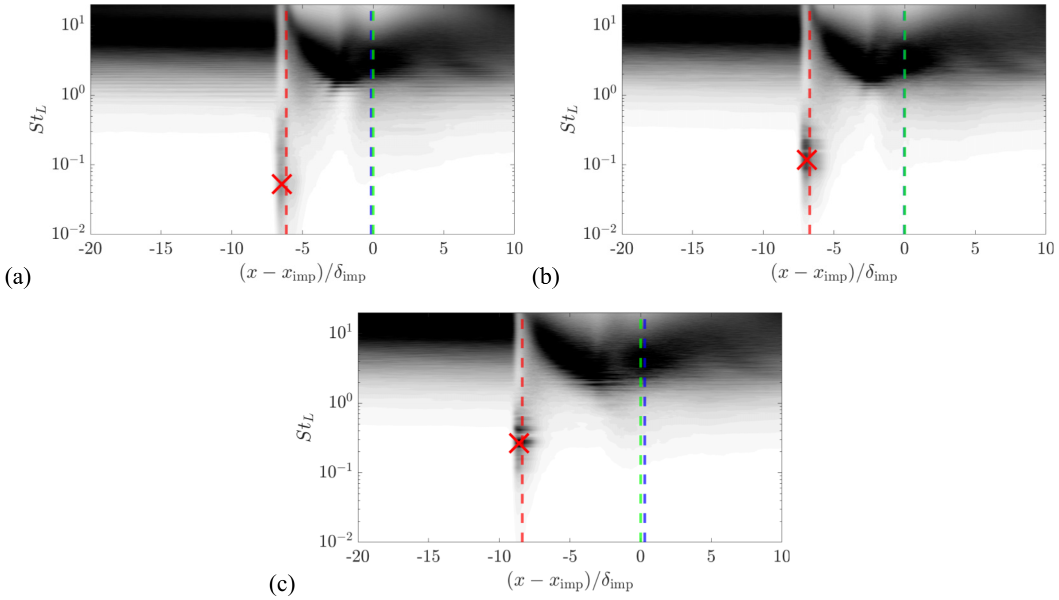

FIG. 15. Premultiplied, normalized PSD of wall pressure fluctuations for flow cases G00_T14 (a), G15_T14 (b), and G30_T14 (c). The red line denotes the mean separation location, the green line the nominal shock impingement location, and the cyan line the mean reattachment location. Red crosses mark the position of the low-frequency peaks near the separation line.

$p'_w(x_{\text{sep}}, z, t)$ is Fourier transformed in the spanwise direction and in time as

$$\hat{p}_i(\kappa_z, \omega) = \int_0^{\mathscr{T}_w} \int_0^{L_z} p'_w(x_{\text{sep}}, z, t) w_H(t) e^{-i(\kappa_z z - \omega t)}\, \mathrm{d}z\, \mathrm{d}t, \tag{14}$$

where $\mathscr{T}_w$ is the time duration of each segment and $w_H(t)$ the Hamming window. The wave-number-frequency spectrum is then obtained by averaging the power-spectral densities

$$S_{pp}(\kappa_z, \omega) = \frac{1}{M} \sum_{i=1}^{M} \hat{p}_i(\kappa_z, \omega) \hat{p}_i^*(\kappa_z, \omega) \tag{15}$$

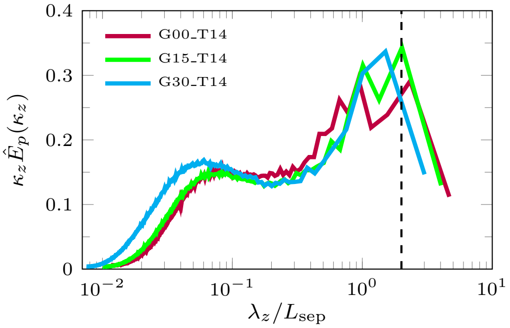

FIG. 16. Premultiplied, spanwise PSD of wall pressure fluctuations at the mean separation line, for various sweep angles. The spanwise wavelength λ_z is scaled by the separation length. $\kappa_z = 2\pi/\lambda_z$ is the spanwise wave number. The dashed line marks $\lambda_z = 2L_{\text{sep}}$.

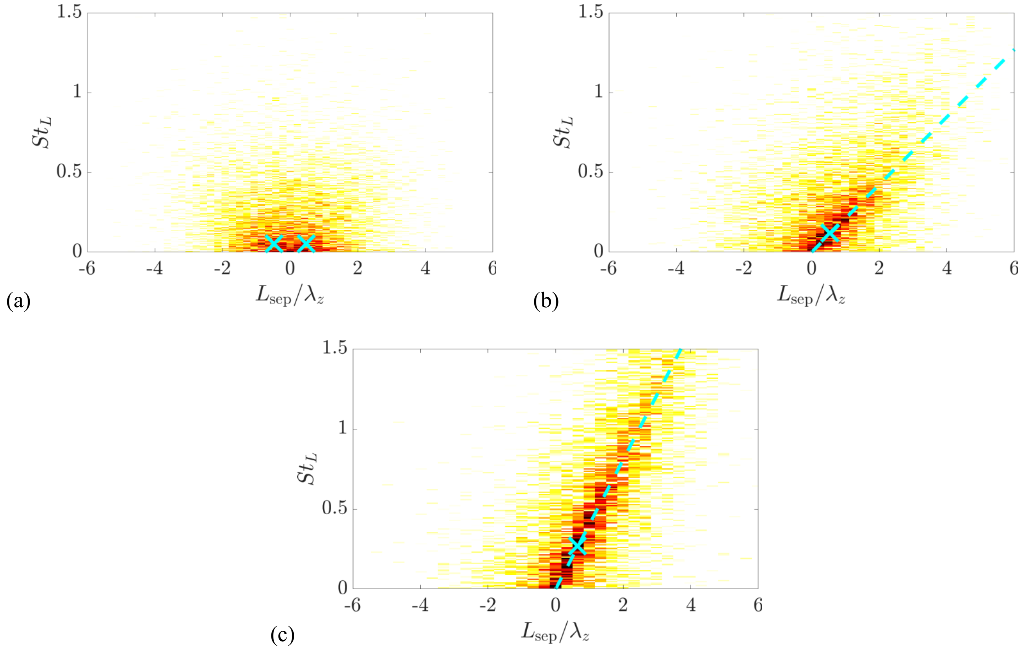

FIG. 17. Contour plots of frequency/wave number spectra of the wall pressure at the mean separation location. Dashed lines denote the linear relationship for the circular frequency $\omega = \kappa_z w_c$, with convection velocity $w_c = 0.7u_{0,x} \tan \gamma_0$. (a) $\gamma_0 = 0°$; (b) $\gamma_0 = 15°$; (c) $\gamma_0 = 30°$. The cyan crosses mark the position of the low-frequency peaks.

where $(\cdot)^*$ indicates complex conjugate and M the number of segments. In practice, this quantity is obtained by the discrete data set of instantaneous wall pressure by evaluating the window average of the pressure PSDs in each segment, which in turn are calculated using spatiotemporal fast Fourier transform. The S_{pp} distribution is then suitably normalized to be consistent with the spanwise-averaged spectra in Fig. 18. Whereas no clear organization is observed in nonswept SBLI [Fig. 17(a)], distinct linear clustering of the PSD is found in swept interactions, which becomes more evident at high sweep angles, and which is a clear indication of the presence of disturbances

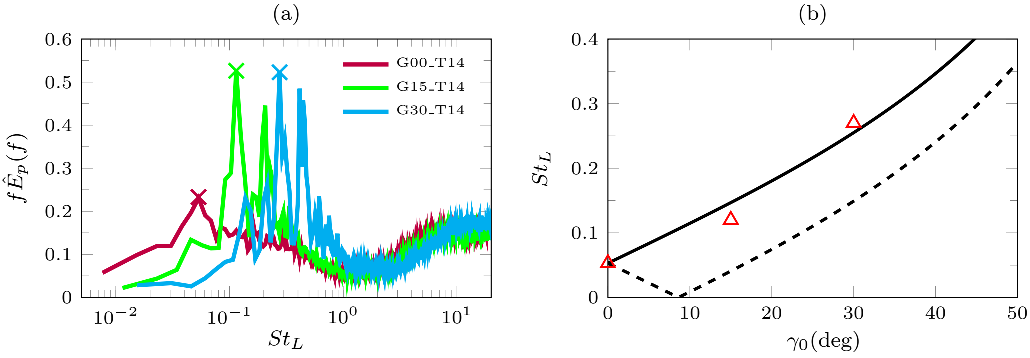

FIG. 18. (a) Premultiplied, normalized frequency spectra of wall pressure fluctuations at the mean separation line, for various sweep angles. Peaks are marked with crosses. (b) Peak frequency as a function of sweep angle: the solid and dashed lines denote the prediction of Eq. (16). Numerical values are marked with triangles.

traveling at a definite phase speed w_c, without any obvious dispersion. In particular, data fitting yields the same convection velocity found by Ceci *et al.* [42], i.e., $w_c \approx 0.7u_{0,z} = 0.7u_{0,x} \tan \gamma_0$.

The typical frequencies of the spanwise traveling pressure perturbations described above are gathered by Fig. 18(a), which reports the premultiplied, normalized pressure PSD at mean separation line. All distributions exhibit a bump at high frequency, which is associated with the boundary layer turbulence dynamics. In addition, they show prominent peaks at much lower frequency, which shift to the right and increase in magnitude as the sweep angle increases. Quantitative comparison of the computed peak frequencies with the formula

$$\mathrm{St}_L = \left| \mathrm{St}_{L,0} \pm \frac{k_\eta \tan \gamma_0}{\alpha} \right|, \tag{16}$$

obtained by Ceci *et al.* [42] for supersonic interactions, is presented in Fig. 18(b). The prediction is quite good by using the same fitting parameters ($k_\eta = 0.7$, $\alpha = 2$) as we found for the supersonic case.

The presence of large-scale unsteadiness in the interaction region can be further elucidated by applying the POD technique, to extract a set of characteristic spatial functions $w_j(x, z)$ which optimally describe the wall pressure fluctuations. In particular, the goal of the analysis is to obtain the spatial shape of the dominant structures in the neighborhood of the mean separation location. In this framework, the unsteady pressure field is expanded as

$$p'(x, z, t) = \sum_{j=1}^{\infty} a_j(t) w_j(x, z). \tag{17}$$

Here $a_j(t) = \langle p'(x, z, t), w_j(x, z)\rangle$ is the jth temporal coefficient (with $\langle\cdot, \cdot\rangle$ a suitable scalar product in a Hilbert space). As customary in many applications of POD to fluid flows, we follow the snapshot method [51], whereby the data at a given time t_j are arranged into a column vector $\mathbf{q}_j$, $j = 1, \dots, M$, with M the number of snapshots, and the snapshot matrix is defined as $\mathbf{Q} = [\mathbf{q}_1, \mathbf{q}_2, \dots, \mathbf{q}_M]$. The discrete temporal coefficients ψ_j are then obtained by solving the discrete eigenvalue problem

$$\mathbf{Q}^T \mathbf{W} \mathbf{Q} \psi_j = \lambda_j \psi_j. \tag{18}$$

The corresponding POD modes are then recovered as

$$\boldsymbol{\phi}_j = \mathbf{F}^{-1} \mathbf{Q} \psi_j \frac{1}{\sqrt{\lambda_j}}, \tag{19}$$

where $\mathbf{W}$ is a positive-definite Hermitian matrix defining the spatial weights and $\mathbf{W} = \mathbf{F}^T \mathbf{F}$ is its Cholesky decomposition. In this specific flow case, solving Eq. (18) with an unitary weight matrix, which is appropriate for a single thermodynamic variable discretized on an uniform grid, results in a multitude of high-frequency leading modes, with large-scale unsteadiness confined to high-order modes. This finding is consistent with the sharp rise of pressure loads in the rear part of the interaction region as observed in Figs. 2(a) and 4(a).

In order to isolate the low-energy, low-frequency dynamics occurring in the vicinity of the mean separation point, we consider a nonunitary weight matrix, defined as

$$\mathbf{W} = \mathrm{diag}\left(p_0^2/\overline{p}_{w,i}^2\right), \quad i = 1, \dots, N_x \times N_z, \tag{20}$$

which penalizes pressure fluctuations downstream of the mean pressure plateau. Figure 19 depicts the shapes of the leading POD modes for $\gamma_0 = 0^\circ$ and $\gamma_0 = 30^\circ$, along with the PSD of the associated temporal coefficients. Large-scale corrugations clearly emerge in the mean separation region, whose characteristic wavelength and frequency conform with those found through the spectral analysis. At reattachment pressure corrugations appear, which feature the same spanwise wavelength as at the separation point. In the unswept case, perfect phase opposition between those corrugations can be observed, which can be interpreted as the signature of two-dimensional

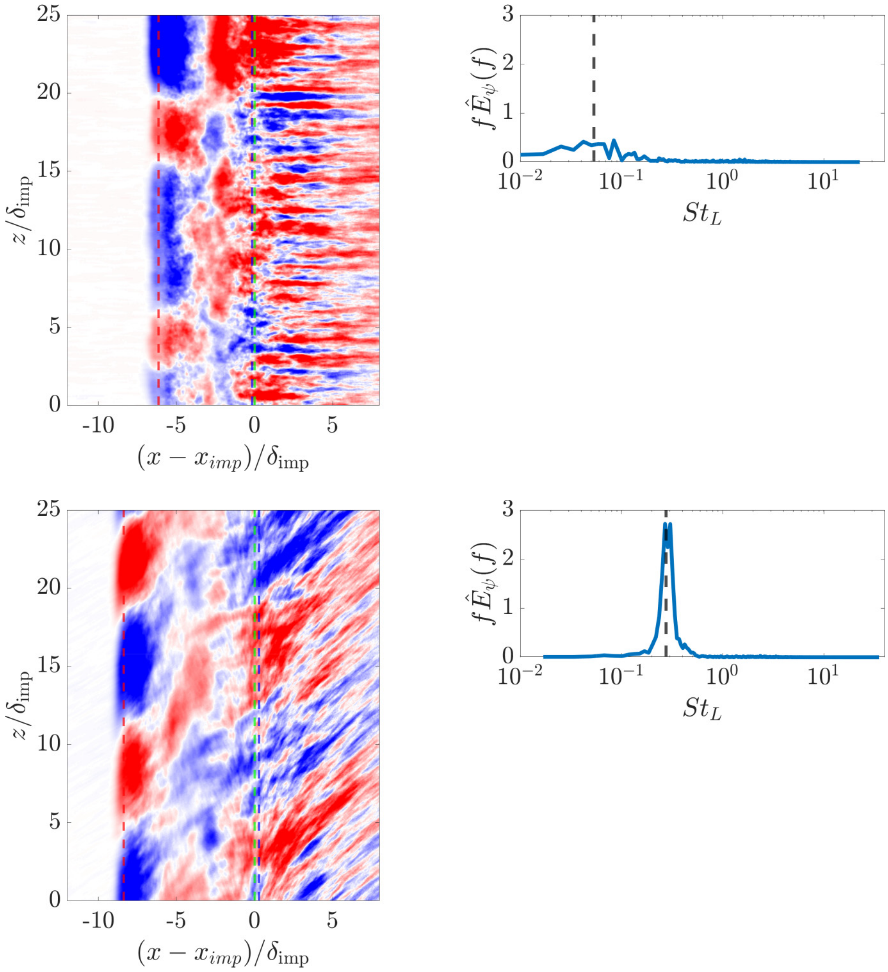

(a)

(b)

FIG. 19. Leading POD mode $\phi_1(x, z)$ (left panel) and premultiplied PSD of associated temporal coefficient $\psi_1(t)$ (right panel) of wall pressure in the interaction region. (a) Case G00_T14, (b) case G30_T14.

breathing. In the swept case, wave peaks and troughs upstream of the reattachment point appear to be aligned at an angle $\gamma \approx 50^\circ$, in agreement with Fig. 12(c). This observation is consistent with the occurrence of spanwise drift of pressure perturbations within separation zone in swept interaction cases. The POD modes also detect additional coherent pressure oscillations past reattachment, with spanwise much smaller wavelength than that typical of the large-scale unsteadiness, which could be related to the low-frequency end of disturbances from the mixing layers surrounding the separation bubble. In the swept case, those disturbances are inclined with respect to the streamwise axis, following the mean flow direction shown in Fig. 11.

V. CONCLUSIONS

We have carried out high-fidelity simulations of hypersonic shock/boundary layer interactions of impinging type, and focused on the effect of an imposed crossflow. The analysis of the mean fields supports the notion that the extent of the separation bubble increases in the presence of crossflow, in agreement with previous supersonic studies [40,41]. Inspection of the flow angle following the dividing streamline reveals uplift and subsequent downlift of fluid particles far from the wall, accompanied by a spanwise shift. On the other hand, near-wall particles are found to travel backwards from the reattachment to the separation line, at a crossflow velocity which is much higher than the streamwise one. This effect is noticed for instance in the friction lines for the largest crossflow angle (see Fig. 11), showing that the flow midway of the bubble is essentially aligned with the spanwise direction.

The numerical data allow to draw some conclusions regarding assumptions and validity of the free-interaction theory [54]. In particular, we find that the most appropriate definition of the starting location of the interaction is based on the maximum wall pressure gradient, which yields more universal distributions than use of the zero crossing of the friction coefficient. As for the relevant length scale to be used for normalization, not surprisingly we find that choosing a typical upstream boundary layer thickness yields good universality up to the mean separation point position, whereas use of the separation length yields improved collapse of the distributions further downstream. The analysis further corroborates the notion that the commonly quoted plateau value of the similarity function ($F = 6$) is attained only in flow cases featuring very strong interactions, and none of the hypersonic cases herein considered qualify for that.

Analysis of the wall pressure signal has been carried out in terms of the frequency/wave number spectra and proper orthogonal decomposition, and has led to full characterization of the low-frequency unsteadiness observed in the interaction region. We find that the typical low-frequency disturbances correspond to spanwise perturbations with typical wavelength of about two times the size of the reversed flow region. In the case of swept interactions disturbances in this region travel at about 70% of the crossstream velocity, resulting in apparent shift to higher frequencies, which we found to be very well predicted by the model developed by Ceci *et al.* [42].

Interestingly, POD is capable of detecting additional structures in the rear part of the separation bubble, whose motion appears to be correlated with rippling of the separation line. This observation, linked with the observed streamlines/friction lines patterns opens the possibility of extending physical analysis developed for two-dimensional breathing to the three-dimensional interactions with cylindrical symmetry.

Further ramification of this work might include considering cases with strong wall cooling and/or chemical nonequilibrium typical of hypersonic flight, and establish the influence of those physical effects on large-scale unsteadiness.

ACKNOWLEDGMENTS

This work was supported by the Air Force Office of Scientific Research under Grants No. FA9550-23-1-0228 and No. FA8655-23-1-7016. We acknowledge that the results reported in this paper have been achieved with computational resources of "IscrB_DSHOW" and "IscrB_THOR" projects, using the EuroHPC Joint Undertaking Research Infrastructure resource Leonardo based at CINECA, Casalecchio di Reno, Italy, and computational resources of Regular Access Project "THOR" on the EuroHPC Joint Undertaking Infrastructure resource Karolina-GPU, based at IT4Innovations National Supercomputing Center at VSB, Technical University of Ostrava, Czech Republic.

---

[1] T. A. Heppenheimer, *Facing the heat barrier: A history of hypersonics* (NASA, Washington, DC, 2006), Vol. 4232.

[2] J. J. Bertin and R. M. Cummings, Fifty years of hypersonics: Where we've been, where we're going, Prog. Aerosp. Sci. **39**, 511 (2003).

[3] D. Sziroczak and H. Smith, A review of design issues specific to hypersonic flight vehicles, Prog. Aerosp. Sci. **84**, 1 (2016).

[4] J. Urzay, Supersonic combustion in air-breathing propulsion systems for hypersonic flight, Annu. Rev. Fluid Mech. **50**, 593 (2018).

[5] D. M. Van Wie, Hypersonics: Past, present, and potential future, John Hopkins APL Technical Digest **35**, 335 (2021).

[6] M. Holden, A review of aerothermal problems associated with hypersonic flight, in *24th Aerospace Sciences Meeting*, AIAA Paper No. 1986-0267 (AIAA, Reno, Nevada, 1986),p. 267.

[7] D. S. Dolling, Fifty years of shock-wave/boundary-layer interaction research: What next? AIAA J. **39**, 1517 (2001).

[8] H. Babinsky and J. Harvey, *Shock Wave-Boundary-Layer Interactions*, Cambridge Aerospace Series Vol. 32 (Cambridge University Press, Cambridge, 2011).

[9] N. Clemens and V. Narayanaswamy, Low-frequency unsteadiness of shock wave/turbulent boundary layer interactions, Annu. Rev. Fluid Mech. **46**, 469 (2014).

[10] D. Gaitonde and M. Adler, Dynamics of three-dimensional shock-wave/boundary-layer interactions, Annu. Rev. Fluid Mech. **55**, 291 (2023).

[11] P. S. Volpiani, M. Bernardini, and J. Larsson, Effects of a nonadiabatic wall on hypersonic shock/boundary-layer interactions, Phys. Rev. Fluids **5**, 083401 (2020).

[12] C. M. Helm and M. P. Martin, Scaling of hypersonic shock/turbulent boundary layer interactions, Phys. Rev. Fluids **6**, 074607 (2021).

[13] M. Yu, D. Sun, Q. Zhou, P. Liu, and X. Yuan, Coherent structures and turbulent model refinement in oblique shock/hypersonic turbulent boundary layer interactions, Phys. Fluids **35**, 086125 (2023).

[14] S. Piponniau, J. P. Dussauge, J. F. Debiève, and P. Dupont, A simple model for low-frequency unsteadiness in shock-induced separation, J. Fluid Mech. **629**, 87 (2009).

[15] B. Ganapathisubramani, N. Clemens, and D. Dolling, Low-frequency dynamics of shock-induced separation in a compression ramp interaction, J. Fluid Mech. **636**, 397 (2009).

[16] J.-P. Dussauge, P. Dupont, and J.-F. Debiève, Unsteadiness in shock wave boundary layer interactions with separation, Aero. Sci. Tech. **10**, 85 (2006).

[17] S. Pirozzoli and F. Grasso, Direct numerical simulation of impinging shock wave turbulent boundary layer interaction at $M = 2.25$, Phys. Fluids **18**, 065113 (2006).

[18] E. Touber and N. Sandham, Large-eddy simulation of low-frequency unsteadiness in a turbulent shock-induced separation bubble, Theor. Comput. Fluid Dyn. **23**, 79 (2009).

[19] V. Pasquariello, S. Hickel, and N. Adams, Unsteady effects of strong shock-wave/boundary-layer interaction at high Reynolds number, J. Fluid Mech. **823**, 617 (2017).

[20] J. W. Nichols, J. Larsson, M. Bernardini, and S. Pirozzoli, Stability and modal analysis of shock/boundary layer interactions, Theor. Comput. Fluid Dyn. **31**, 33 (2017).

[21] A. Grébert, J. Bodart, S. Jamme, and L. Joly, Simulations of shock wave/turbulent boundary layer interaction with upstream micro vortex generators, Int. J. Heat Fluid Flow **72**, 73 (2018).

[22] M. Grilli, P. Schmid, S. Hickel, and N. Adams, Analysis of unsteady behaviour in shockwave turbulent boundary layer interaction, J. Fluid Mech. **700**, 16 (2012).

[23] S. Priebe, J. Tu, C. Rowley, and M. P. Martín, Low-frequency dynamics in a shock-induced separated flow, J. Fluid Mech. **807**, 441 (2016).

[24] J. Hao, On the low-frequency unsteadiness in shock wave–turbulent boundary layer interactions, J. Fluid Mech. **971**, A28 (2023).

[25] G. S. Settles, J. J. Perkins, and S. M. Bogdonoff, Investigation of three-dimensional shock/boundary-layer interactions at swept compression corners, AIAA J. **18**, 779 (1980).

[26] M. E. Erengil and D. S. Dolling, Effects of sweepback on unsteady separation in Mach 5 compression ramp interactions, AIAA J. **31**, 302 (1993).

[27] K. Sabnis and H. Babinsky, A review of three-dimensional shock wave–boundary-layer interactions, Prog. Aerosp. Sci. **143**, 100953 (2023).

[28] L. Vanstone, M. Saleem, S. Seckin, and N. Clemens, Role of boundary-layer on unsteadiness on a Mach 2 swept-ramp shock/boundary-layer interaction using 50 kHz PIV, in *55th AIAA Aerospace Sciences Meeting*, AIAA Paper No. 2017-0757 (AIAA, Texas, 2017).

[29] M. Adler and D. Gaitonde, Unsteadiness in shock/turbulent-boundary-layer interactions with open flow separation, in *2018 AIAA Aerospace Sciences Meeting*, AIAA Paper No. 2018-2075 (AIAA, Florida, 2018).

[30] M. Adler and D. Gaitonde, Dynamics of strong swept-shock/turbulent-boundary-layer interactions, J. Fluid Mech. **896**, A29 (2020).

[31] J. Zhang, T. Guo, G. Dang, and X. Li, Direct numerical simulation of shock wave/turbulent boundary layer interaction in a swept compression ramp at Mach 6, Phys. Fluids **34**, 116110 (2022).

[32] J. D. Schmisseur and D. S. Dolling, Fluctuating wall pressures near separation in highly swept turbulent interactions, AIAA J. **32**, 1151 (1994).

[33] D. V. Gaitonde, J. S. Shang, T. J. Garrison, A. A. Zheltovodov, and A. I. Maksimov, Three-dimensional turbulent interactions caused by asymmetric crossing-shock configurations, AIAA J. **37**, 1602 (1999).

[34] N. Arora, L. Mears, and F. Alvi, Unsteady characteristics of a swept-shock/boundary-layer interaction at Mach 2, AIAA J. **57**, 4548 (2019).

[35] M. C. Adler and D. V. Gaitonde, Structure, scale, and dynamics of a double-fin shock/turbulent-boundary-layer interaction at Mach 4, in *AIAA Scitech 2019 Forum*, AIAA Paper No. 2019-0096 (AIAA, 2019).

[36] S. Seckin, L. J. Mears, M. Song, F. Zigunov, P. Sellappan, and F. S. Alvi, Surface properties of double-fin generated shock-wave/boundary-layer interactions, in *AIAA Scitech 2022 Forum*, AIAA Paper No. 2022-0701 (AIAA, 2022).

[37] A. Doehrmann, S. Padmanabhan, J. Threadgill, and J. Little, Effect of sweep on the mean and unsteady structures of impinging shock/boundary layer interactions, in *2018 AIAA Aerospace Sciences Meeting*, AIAA Paper No. 2018-2074 (AIAA, 2018).

[38] S. Padmanabhan, J. Maldonado, J. Threadgill, and J. Little, Experimental study of swept impinging oblique shock/boundary-layer interactions, AIAA J. **59**, 140 (2021).

[39] A. Gross and H. Fasel, Numerical investigation of shock boundary-layer interactions, in *54th AIAA Aerospace Sciences Meeting*, AIAA Paper No. 2016-0347 (AIAA, 2016).

[40] M. Di Renzo, N. Oberoi, J. Larsson, and S. Pirozzoli, Crossflow effects on shock wave/turbulent boundary layer interactions, Theor. Comput. Fluid Dyn. **36**, 327 (2022).

[41] J. Larsson, V. Kumar, N. Oberoi, M. Di Renzo, and S. Pirozzoli, Large eddy simulations of idealized shock/boundary-layer interactions with crossflow, AIAA J. **60**, 2767 (2022).

[42] A. Ceci, A. Palumbo, J. Larsson, and S. Pirozzoli, On low-frequency unsteadiness in swept shock wave–boundary layer interactions, J. Fluid Mech. **956**, R1 (2023).

[43] T. Bergier, R. Gojon, M. Fiore, J. Gressier, S. Jamme, and L. Joly, Sweep effects on a canonical shock wave/boundary layer interaction, Int. J. Heat Fluid Flow **104**, 109227 (2023).

[44] M. Vitols, J. R. Groves, J. A. Threadgill, and J. C. Little, Mean flow characterization of swept shock/boundary layer interactions: Isolating the influence of sweep, in *AIAA SCITECH 2024 Forum*, AIAA Paper No. 2024-2553 (AIAA, Orlando, FL, 2024).

[45] M. Bernardini, D. Modesti, F. Salvadore, and S. Pirozzoli, STREAmS: A high-fidelity accelerated solver for direct numerical simulation of compressible turbulent flows, Comput. Phys. Commun. **263**, 107906 (2021).

[46] S. Pirozzoli, Generalized conservative approximations of split convective derivative operators, J. Comput. Phys. **229**, 7180 (2010).

[47] A. Wray, Minimal storage time advancement schemes for spectral methods, NASA Ames Research Center, California, Report No. MS 202 (1990).

[48] A. Ceci, A. Palumbo, J. Larsson, and S. Pirozzoli, Numerical tripping of high-speed turbulent boundary layers, Theor. Comput. Fluid Dyn. **36**, 865 (2022).

[49] A. Ceci and S. Pirozzoli, Natural grid stretching for dns of compressible wall-bounded flows, J. Comput. Phys.: X **17**, 100128 (2023).

[50] E. Schülein, Skin friction and heat flux measurements in shock/boundary layer interaction flows, AIAA J. **44**, 1732 (2006).

[51] L. Sirovich, Turbulence and the dynamics of coherent structures. I. Coherent structures, Quart. Appl. Math. **45**, 561 (1987).

[52] P. Schlatter and R. Örlü, Assessment of direct numerical simulation data of turbulent boundary layers, J. Fluid Mech. **659**, 116 (2010).

[53] L. Duan, I. Beekman, and M. Martin, Direct numerical simulation of hypersonic turbulent boundary layers. Part 2. Effect of wall temperature, J. Fluid Mech. **655**, 419 (2010).

[54] D. R. Chapman, D. M. Kuehn, and H. K. Larson, Investigation of separated flows in supersonic and subsonic streams with emphasis on the effect of transition, NACA Technical Report (NACA, Washington, 1958).

[55] P. Carrière, M. Sirieix, and J.-L. Solignac, Similarity properties of the laminar or turbulent separation phenomena in a non-uniform supersonic flow, in *Applied Mechanics: Proceedings of the Twelfth International Congress of Applied Mechanics, Stanford University, 1968 (IUTAM Symposia)* (Springer, Berlin, Heidelberg, 1969).

[56] A. F. Charwat, Supersonic flows with imbedded separated regions, in *Advances in Heat Transfer*, edited by J. P. Hartnett and T. F. Irvine (Elsevier, 1970), Vol. 6, pp. 1–132.

[57] J. Matheis and S. Hickel, On the transition between regular and irregular shock patterns of shock-wave/boundary-layer interactions, J. Fluid Mech. **776**, 200 (2015).

[58] J. Délery, J. G. Marvin, and E. Reshotko, *Shock-Wave Boundary Layer Interactions* (AGARD, Neuilly-sur-Seine, France, 1986).

[59] J. Erdos and A. Pallone, Shock-boundary layer interaction and flow separation, in *Proceedings of the 1962 Heat Transfer and Fluid Mechanics Institute*, Vol. 15 (Stanford University Press, Stanford, CA, 1962), pp. 239–254.

[60] H. Choi and P. Moin, On the space-time characteristics of wall-pressure fluctuations, Phys. Fluids **2**, 1450 (1990).